A New Formulation of the Spectral Energy Budget of the Atmosphere, with Application to Two High-Resolution General Circulation Models

PIERRE AUGIER AND ERIK LINDBORG

Linné Flow Centre, KTH Mechanics, Stockholm, Sweden

(Manuscript received 15 October 2012, in final form 13 February 2013)

ABSTRACT

A new formulation of the spectral energy budget of kinetic and available potential energies of the atmosphere is derived, with spherical harmonics as base functions. Compared to previous formulations, there are three main improvements: (i) the topography is taken into account, (ii) the exact three-dimensional advection terms are considered, and (iii) the vertical flux is separated from the energy transfer between different spherical harmonics. Using this formulation, results from two different high-resolution GCMs are analyzed: the Atmospheric GCM for the Earth Simulator (AFES) T639L24 and the European Centre for Medium-Range Weather Forecasts (ECMWF) Integrated Forecast System (IFS) T1279L91. The spectral fluxes show that the AFES, which reproduces quite realistic horizontal spectra with a $k^{-5/3}$ inertial range at the mesoscales, simulates a strong downscale energy cascade. In contrast, neither the $k^{-5/3}$ vertically integrated spectra nor the downscale energy cascade are produced by the ECMWF IFS.

1. Introduction

The atmospheric horizontal spectra of velocity components and temperature show a robust $k^{-5/3}$ range at the mesoscales (10–500 km) (Nastrom and Gage 1985). This power law and the corresponding one for the horizontal second-order structure functions $r^{2/3}$ are obtained from signals measured in the troposphere and the stratosphere over both land and sea (e.g., Frehlich and Sharman 2010). It still remains a challenge to reproduce these results in simulations. Some general circulation models (GCMs) (e.g., Koshyk and Hamilton 2001; Hamilton et al. 2008) and mesoscale numerical weather prediction (NWP) models (Skamarock 2004) reproduce quite realistic mesoscale spectra. Other GCMs, as for example the European Centre for Medium-Range Weather Forecasts (ECMWF)'s weather prediction model Integrated Forecast System, produce mesoscale spectra significantly steeper and with smaller magnitude than the measured ones, even with relatively high-resolution versions (e.g., Shutts 2005). The inability of some GCMs to simulate realistic mesoscale spectra must have important consequences in terms of predictability (Vallis 2006), dispersiveness of ensemble prediction systems (Palmer 2001), and, evidently, mesoscale NWP.

Even though one can now simulate realistic mesoscale spectra, it is still unclear what physical mechanisms produce them. Theoretically, the only convincing explanation of the $k^{-5/3}$ power law is the hypothesis that it is produced by an upscale or downscale energy cascade with a constant energy flux through the scales. Therefore, most of the different theories proposed are based on the hypothesis of an energy cascade: upscale cascade due to 2D stratified turbulence (Gage 1979; Lilly 1983) or downscale cascade due to internal gravity waves (Dewan 1979; Smith et al. 1987), quasigeostrophic dynamics (Tung and Orlando 2003), surface quasigeostrophic dynamics (Tulloch and Smith 2009), or 3D strongly stratified turbulence (Lindborg 2006).

The principle of energy conservation strongly constrains the dynamics of the atmosphere. To explain the maintenance of the general circulation, Lorenz (1955) developed the concept of available potential energy (APE) and derived an approximate expression proportional to the variance of the temperature fluctuation. His work has laid the foundations for several studies investigating APE (e.g., Boer 1989; Shepherd 1993; Siegmund 1994; Molemaker and McWilliams 2010) and the atmospheric energy budget through diagnostics of data from global meteorological analysis and GCMs (e.g., Boer and

Corresponding author address: Pierre Augier, Linné Flow Centre, KTH, Department of Mechanics, SE-100 44 Stockholm, Sweden.
E-mail: pierre.augier@mech.kth.se

DOI: 10.1175/JAS-D-12-0281.1

Lambert 2008; Steinheimer et al. 2008). Because of the multiscale nature of atmospheric motions, spectral analysis can reveal valuable pieces of information from the data (Fjørtoft 1953) and have therefore become a standard method for diagnostics. However, drawbacks of different used formulations of the spectral energy budget severely limit the results. First, the attention has been focused on the budget of kinetic energy (KE) so that in many studies the APE budget is not considered. Most studies investigate only the budget integrated over the total height of the atmosphere and thus the vertical fluxes of energy are not computed. Another very important limitation is that most studies are based on the formulation proposed by Fjørtoft (1953), in which only the purely horizontal and nondivergent flow is considered (e.g., Burrows 1976; Boer and Shepherd 1983; Shepherd 1987; Boer 1994; Straus and Ditlevsen 1999; Burgess et al. 2013). This approximation is justified for the very large scales of the atmosphere for which the divergence is indeed very small. However, the approximation may lead to large errors at the mesoscales. Atmospheric measurements show that divergent and rotational spectra are of the same order (Lindborg 2007) and atmospheric simulations produce divergent spectra of the same order of magnitude as rotational spectra at the mesoscales (e.g., Hamilton et al. 2008; Burgess et al. 2013). Moreover, these results are consistent with theoretical results showing that strongly stratified and weakly rotating flows tend to evolve toward states in which the divergent and rotational components are of the same order of magnitude (Billant and Chomaz 2001; Lindborg and Brethouwer 2007; Augier et al. 2012). Therefore, the spectral energy budget formulations based on the two-dimensional vorticity equation cannot capture the dynamics at the mesoscales.

There is no theoretical obstacle in considering the exact three-dimensional advection including both rotational and divergent components of the flow. Lambert (1984) has developed a formulation of the spectral energy budget considering both KE and APE and taking into account the exact advection term. However, the diagnostics was integrated over the total height of the atmosphere so vertical fluxes were not considered. Koshyk and Hamilton (2001) performed a diagnostic of the equation for the KE spectrum (the APE budget was not investigated). The exact advection was computed but the vertical flux was not separated from the energy transfer between spherical harmonics, so it was impossible to define spectral fluxes in a conservative way. Koshyk and Hamilton (2001) separated the spectral pressure term into adiabatic conversion and vertical flux. However, the separation was only approximate. Moreover, as in all previous studies on the spectral energy budget, the topography was neglected. Recently, Brune and Becker (2013) have investigated the effect of the vertical resolution in a mechanistic GCM. Just as in Koshyk and Hamilton (2001), all of the terms in the kinetic spectral energy equation were computed at different pressure levels and it was demonstrated that they balance each other. However, spectral fluxes were defined in a nonconservative way and actually also included vertical fluxes.

To investigate the energetics of the mesoscales simulated by GCMs, it would be desirable to formulate the spectral energy budget considering both KE and APE, taking the topography into account and making an exact separation of the advection terms into spectral transfer and vertical flux and a corresponding separation of the pressure term into adiabatic conversion and vertical flux. A formulation meeting these requirements is derived in section 2. In section 3, results from two high-resolution GCMs are analyzed.

2. Formulation of the spectral energy budget

a. Governing equations in p coordinates

The analysis is performed in pressure coordinates in which variables are functions of time t, longitude λ, latitude φ (the horizontal coordinates are denoted by $\mathbf{x}_h$), and pressure p. The main advantage of the p coordinates is that mass conservation can be expressed in the same way as for an incompressible fluid: $\nabla \cdot \mathbf{v} = 0$, where $\nabla = (\nabla_h, \partial_p)$ is the gradient operator and $\mathbf{v} = (\mathbf{u}, \omega)$ is the total velocity [∇_h is the horizontal gradient operator, $\mathbf{u}$ is the horizontal velocity, and $\omega = \mathrm{D}_t p$ is the pressure velocity (D_t is the material derivative)]. The hydrostatic equation is $\partial_p \Phi = -\alpha = -RT/p$, where Φ is the geopotential and α is the volume per unit mass.

In the p coordinates, the evolution equations can be written as

$$\mathrm{D}_t \mathbf{u} = -f(\varphi)\mathbf{e}_z \wedge \mathbf{u} - \nabla_h \Phi + \mathrm{D}_{\mathbf{u}}(\mathbf{u}), \tag{1}$$

$$\mathrm{D}_t H = \omega\alpha + \dot{Q} + \mathrm{D}_H(H), \tag{2}$$

where $f(\varphi)$ is the Coriolis parameter, $\mathbf{e}_z$ is the upward (radial) unit vector, $H = c_p T$ is the enthalpy per unit mass, $\dot{Q}$ is the rate of production of internal energy by heating, and $\mathrm{D}_{\mathbf{u}}(\mathbf{u})$ and $\mathrm{D}_H(H)$ are diffusion terms. The thermodynamic equation (2) can be rewritten as a conservation equation for the potential temperature $\theta = \Lambda(p)T$, with $\Lambda(p) = (p_0/p)^{\chi}$, $p_0 = 1$ bar, and $\chi = R/c_p \simeq 2/7$. For simplicity, the corrections related to the vapor content are neglected. However, the latent heat release is taken into account through the associated heating.

The main drawback of the p coordinates is the complication related to the lower boundary condition (the topography pierces the lower pressure levels). It can be overcome with the formalism developed by Boer (1982) (see appendix A) in which the dynamical equations can be written as

$$\partial_t \tilde{\mathbf{u}} = -\mathbf{v}\cdot\nabla\tilde{\mathbf{u}} - f(\varphi)\mathbf{e}_z \wedge \tilde{\mathbf{u}} - \beta\nabla_h\Phi + \beta \mathrm{D}_{\mathbf{u}}(\mathbf{u}), \quad (3)$$

$$\partial_t \tilde{\theta}' = -\mathbf{v}\cdot\nabla\tilde{\theta}' - \tilde{\omega}\partial_p\langle\theta\rangle_r + \tilde{Q}_\theta - \beta\partial_t\langle\theta\rangle_r + \beta \mathrm{D}_\theta(\theta), \quad (4)$$

where $\mathrm{D}_\theta(\theta)$ is a diffusion term, $Q_\theta \equiv \Lambda(p)\dot{Q}/c_p$, and $\tilde{\mathbf{u}} = \beta(\mathbf{x}_h, p)\mathbf{u}$, with $\beta(\mathbf{x}_h, p)$ equal to one above the surface and to zero below. The potential temperature fluctuation $\tilde{\theta}'$ is defined as $\tilde{\theta}' = \tilde{\theta} - \beta\langle\theta\rangle_r$, where $\langle\theta\rangle_r = \langle\beta\theta\rangle/\langle\beta\rangle$ is the representative mean—that is, the mean over regions above the surface (the angle brackets denote the mean over a pressure level).

b. Kinetic and available potential energy forms

Lorenz (1955) showed that the sum of the globally integrated KE and APE is approximately conserved. The mean energies per unit mass are $E_K(p) = \langle|\tilde{\mathbf{u}}|^2\rangle/2$ and $E_A(p) = \gamma(p)\langle\tilde{\theta}'^2\rangle/2$, with $\gamma(p) = R/[-\Lambda(p)p\partial_p\langle\theta\rangle_r]$. The energy budget can be written as

$$\partial_t E_K(p) = C(p) + \partial_p F_{K\uparrow}(p) - D_K(p) + S(p), \quad (5)$$

$$\partial_t E_A(p) = G(p) - C(p) + \partial_p F_{A\uparrow}(p) - D_A(p) + J(p), \quad (6)$$

where $G(p) = \gamma(p)\langle\tilde{\theta}'\tilde{Q}'_\theta\rangle$ is forcing by heating (differential heating at very large scales and latent heat release), $C(p) = -\langle\tilde{\omega}\tilde{\alpha}\rangle$ is conversion of APE to KE, $F_{A\uparrow}(p) = -\gamma(p)\langle\omega\tilde{\theta}'^2\rangle/2$ and $F_{K\uparrow}(p) = -\langle\omega|\tilde{\mathbf{u}}|^2\rangle/2 - \langle\tilde{\omega}\tilde{\Phi}\rangle$ are vertical fluxes, and $D_K(p)$ and $D_A(p)$ are diffusion terms. The last terms in Eqs. (5) and (6), $S(p) = -\langle\delta\partial_t(p_s\Phi_s)\rangle$ and $J(p) = (\partial_p\gamma)\langle\omega\tilde{\theta}'^2\rangle/2 - \langle\beta^2\rangle\langle\omega\rangle_r\langle\alpha\rangle_r$, correspond to adiabatic processes that do not conserve the sum of the KE and the Lorenz APE. However, when integrated over the whole atmosphere, these terms are negligible so that the sum of the total kinetic energy and the total Lorenz APE is approximately conserved. Siegmund (1994) showed that the globally integrated exact APE and Lorenz APE differ by less than 3%. In appendix B, we show how Eqs. (5) and (6) can be related to the equation of total energy conservation.

c. Spectral analysis based on spherical harmonic transform

For clarity, the spectral energy budget is here derived for levels above the topography for which $\beta(\mathbf{x}_h, p) = 1$. In this section, we do not include the nonconservative term corresponding to $J(p)$ (i.e., we considered γ as a constant). The general formulas used for the numerical computations are given in appendix A. Each scalar function defined on the sphere can be expanded as a sum of spherical harmonics functions $Y_{lm}(\mathbf{x}_h)$, which are the normalized eigenfunctions of the horizontal Laplacian operator on the sphere: $|\nabla_h|^2 Y_{lm} = -l(l+1)Y_{lm}/a^2$ and $\langle Y^*_{l'm'}Y_{lm}\rangle = \delta_{ll'}\delta_{mm'}$, where the star denotes the complex conjugate and l and m are the total and zonal wavenumbers [for details, see Boer (1983)]. The potential temperature fluctuation is written as

$$\theta'(\mathbf{x}_h, p) = \sum_{l\geq 0}\sum_{-l\leq m\leq l}\theta'_{lm}(p)Y_{lm}(\mathbf{x}_h), \quad (7)$$

and the other scalar variables are written in the corresponding way. It follows that the mean over a pressure level of the product of two functions can be written as

$$\langle\omega\Phi\rangle = \sum_{l\geq 0}\sum_{-l\leq m\leq l}(\omega, \Phi)_{lm}, \quad (8)$$

where, by definition,

$$(\omega, \Phi)_{lm} \equiv \Re\{\omega^*_{lm}\Phi_{lm}\}, \quad (9)$$

with $\Re$ denoting the real part. The spectral APE function can thus be defined as

$$E_A^{lm}(p) = \gamma(p)\frac{(\theta', \theta')_{lm}}{2} = \gamma(p)\frac{|\theta'_{lm}(p)|^2}{2} \quad (10)$$

so as the mean APE at a pressure surface is given by $E_A(p) = \sum_{l,m}E_A^{lm}(p)$.

The meridional and azimuthal components of a vector field on the sphere are multiple valued at the poles because of the coordinate singularity. To expand a vector field in spherical harmonics, it is thus appropriate to decompose it in terms of two scalar functions. For example, the velocity field is decomposed as $\mathbf{u} = \nabla_h \wedge (\psi\mathbf{e}_z) + \nabla_h\chi$, where $\psi(\mathbf{x}_h, p)$ is the spherical streamfunction and $\chi(\mathbf{x}_h, p)$ is the spherical velocity potential. The vertical component of the vorticity is given by $\zeta \equiv \mathrm{rot}_h(\mathbf{u}) \equiv \mathbf{e}_z\cdot(\nabla_h\wedge\mathbf{u}) = \nabla_h^2\psi$ and the horizontal divergence by $d \equiv \mathrm{div}_h(\mathbf{u}) \equiv \nabla_h\cdot\mathbf{u} = \nabla_h^2\chi$. Our formulation is based on a result obtained from the rotational–divergent split. The mean value over a sphere with radius a (in our case the radius of Earth) of the scalar product between two horizontal vector fields $\mathbf{a}$ and $\mathbf{b}$ can be written as

$$\langle\mathbf{a}\cdot\mathbf{b}\rangle = \sum_{l\geq 1}\sum_{-l\leq m\leq l}(\mathbf{a}, \mathbf{b})_{lm}, \quad (11)$$

where, by definition,

$$(\mathbf{a}, \mathbf{b})_{lm} \equiv \frac{a^2}{l(l+1)} \Re\{\mathrm{rot}_h(\mathbf{a})^*_{lm} \mathrm{rot}_h(\mathbf{b})_{lm} + \mathrm{div}_h(\mathbf{a})^*_{lm} \mathrm{div}_h(\mathbf{b})_{lm}\}, \quad (12)$$

which rests on the fact that Y_{lm} are eigenfunctions of the Laplace operator. Here, we have used a similar notation on the LHS of Eqs. (9) and (12). It should be understood that when the two arguments of $(\cdot\,,\cdot)_{lm}$ are scalars, we use Eq. (9) and when the arguments are two vector fields, we use Eq. (12). From Eq. (11), it is clear that the spectral KE function can be defined as

$$E_K^{lm}(p) = \frac{(\mathbf{u}, \mathbf{u})_{lm}}{2} = \frac{a^2(|\zeta_{lm}|^2 + |d_{lm}|^2)}{2l(l+1)}. \quad (13)$$

The spectral energy budget is derived by substituting Eqs. (3) and (4) into the time differentiations of Eqs. (13) and (10); that is, $\partial_t E_K^{[lm]}(p) = (\mathbf{u}, \partial_t \mathbf{u})_{lm}$ and $\partial_t E_A^{[lm]}(p) = \gamma(p)(\theta', \partial_t \theta')_{lm}$, respectively. Reorganizing the different terms, the spectral energy budget can be written as

$$\partial_t E_K^{lm}(p) = C^{lm}(p) + T_K^{lm}(p) + L^{lm}(p) + \partial_p F_{K\uparrow}^{lm}(p) - D_K^{lm}(p), \quad (14)$$

$$\partial_t E_A^{lm}(p) = G^{lm}(p) - C^{lm}(p) + T_A^{lm}(p) + \partial_p F_{A\uparrow}^{lm}(p) - D_A^{lm}(p), \quad (15)$$

where $T_K^{lm}(p)$ and $T_A^{lm}(p)$ are spectral transfer terms due to nonlinear interactions and $L^{lm}(p)$ is a spectral transfer term arising from the Coriolis term. Each of the other terms corresponds to a term in Eqs. (5) and (6).

We first focus on the nonlinear term $-\gamma(\theta', \mathbf{v} \cdot \nabla\theta')_{lm}$. From the expression of $F_{A\uparrow}(p)$ in Eq. (6), it is clear that the APE vertical flux can be written as

$$F_{A\uparrow}^{lm}(p) = -\gamma(\theta', \omega\theta')_{lm}/2. \quad (16)$$

A simple method to obtain the spectral transfer term is to compute the complementary part of the nonlinear term

$$T_A^{lm}(p) = -\gamma(\theta', \mathbf{v} \cdot \nabla\theta')_{lm} + \gamma\partial_p(\theta', \omega\theta')_{lm}/2. \quad (17)$$

It is straightforward to show that the sum over all spherical harmonics of $T_A^{lm}(p)$ is equal to $-\gamma\langle\nabla_h \cdot (\mathbf{u}|\theta'|^2/2)\rangle = 0$, meaning that this transfer term is exactly conservative and only redistributes energy among the different spherical harmonics at a pressure level. The diabatic term, the conversion term, and the APE diffusion term are

$$G^{lm}(p) = \gamma(\theta', Q'_\theta)_{lm}, \quad (18)$$

$$C^{lm}(p) = -(\omega, \alpha)_{lm}, \quad \text{and} \quad (19)$$

$$D_A^{lm}(p) = -\gamma(\theta', \mathrm{D}_\theta[\theta])_{lm}. \quad (20)$$

Using the continuity equation, the hydrostatic equation and the fact that the spherical harmonics are eigenfunctions of the Laplace operator, the pressure term is separated into conversion and vertical flux:[1]

$$-(\mathbf{u}, \nabla_h\Phi)_{lm} = C^{lm}(p) - \partial_p(\omega, \Phi)_{lm}. \quad (21)$$

The total KE vertical flux is the sum of the pressure flux plus the turbulent KE flux

$$F_{K\uparrow}^{lm}(p) = -(\omega, \Phi)_{lm} - (\mathbf{u}, \omega\mathbf{u})_{lm}/2. \quad (22)$$

The nonlinear KE spectral transfer is computed as the complementary part of the nonlinear terms

$$T_K^{lm}(p) = -(\mathbf{u}, \mathbf{v} \cdot \nabla\mathbf{u})_{lm} + \partial_p(\mathbf{u}, \omega\mathbf{u})_{lm}/2, \quad (23)$$

which assures that it conserves energy at a pressure level. The horizontal advection of the horizontal velocity is computed using the relation $\mathbf{u} \cdot \nabla_h\mathbf{u} = \nabla_h|\mathbf{u}|^2/2 + \zeta\mathbf{e}_z \wedge \mathbf{u}$. A transfer term arises from the Coriolis term

$$L^{lm}(p) = -(\mathbf{u}, f[\varphi]\mathbf{e}_z \wedge \mathbf{u})_{lm} = (\psi, \mathrm{rot}_h\{f[\varphi]\mathbf{e}_z \wedge \mathbf{u}\})_{lm} + (\chi, \mathrm{div}_h\{f[\varphi]\mathbf{e}_z \wedge \mathbf{u}\})_{lm}. \quad (24)$$

At the f plane, where f is constant and a Fourier decomposition is used, the corresponding term is zero. Using the definition of the Coriolis parameter $f(\varphi) = f_0 \sin\varphi$ and splitting the velocity in rotational and divergent parts, one can show that

$$L^{lm}(p) = f_0[(\psi, \sin\varphi d + \cos\varphi\partial_\varphi\chi/a^2)_{lm} - (\chi, \sin\varphi\zeta + \cos\varphi\partial_\varphi\psi/a^2)_{lm}]. \quad (25)$$

This implies that the linear transfer does not involve rotational–rotational (or divergence–divergence) interactions.

[1] Koshyk and Hamilton (2001) made a similar but approximate decomposition using the spherical harmonics transforms of the components of the vectors.

To summarize, in contrast to the previous formulations, here, the APE budget is included, the exact three-dimensional advection is considered, and the vertical flux terms and the horizontal spectral transfer terms are exactly separated. Moreover, the topography, which has been neglected in this section for clarity, can consistently be taken into account in the spectral analysis, as shown in appendix A.

d. Vertical integration, summation over zonal wavenumbers, and cumulative summation over total wavenumbers

Since the density strongly varies with height in the atmosphere, we prefer to include the density when we integrate spectral energies over layers, so that our quantities have the dimension of energy rather than energy per unit mass as in most other studies. With the formulation by Boer, this can be done easily even for pressure levels pierced by the topography. The vertically integrated KE spectrum is defined as

$$E_K[l]_{p_t}^{p_b} = \int_{p_t}^{p_b} \frac{dp}{g} \sum_{-l\le m\le l} E_K^{lm}(p). \tag{26}$$

The vertically integrated nonlinear spectral flux of kinetic energy is defined as

$$\Pi_K[l]_{p_t}^{p_b} = \sum_{n\ge l} \int_{p_t}^{p_b} \frac{dp}{g} \sum_{-n\le m\le n} T_K^{nm}(p), \tag{27}$$

and the spectral flux of APE is defined in the corresponding way. When Eqs. (14) and (15) are vertically integrated, divided by g, and summed as in Eq. (27) over all of the spherical harmonics with total wavenumber greater than or equal to l, we obtain

$$\begin{aligned}\partial_t \mathcal{E}_K[l]_{p_t}^{p_b} = {} & \mathcal{C}[l]_{p_t}^{p_b} + \Pi_K[l]_{p_t}^{p_b} + \mathcal{L}[l]_{p_t}^{p_b} + \mathcal{F}_{K\uparrow}[l](p_b) \\ & - \mathcal{F}_{K\uparrow}[l](p_t) - \mathcal{D}_K[l]_{p_t}^{p_b}, \end{aligned} \tag{28}$$

$$\begin{aligned}\partial_t \mathcal{E}_A[l]_{p_t}^{p_b} = {} & \mathcal{G}[l]_{p_t}^{p_b} - \mathcal{C}[l]_{p_t}^{p_b} + \Pi_A[l]_{p_t}^{p_b} + \mathcal{F}_{A\uparrow}[l](p_b) \\ & - \mathcal{F}_{A\uparrow}[l](p_t) - \mathcal{D}_A[l]_{p_t}^{p_b}, \end{aligned} \tag{29}$$

where the terms named $\mathcal{F}_\uparrow[l](p) = \sum_{n\ge l} F_\uparrow[n]$ are cumulative vertical fluxes and each of the other terms is an integrated cumulation of a corresponding term in Eqs. (14) and (15). For example, $\mathcal{E}_K[l]_{p_t}^{p_b} = \sum_{n\ge l} E_K[n]_{p_t}^{p_b}$ is the cumulative kinetic energy and $\mathcal{C}_K[l]_{p_t}^{p_b} = \sum_{n\ge l} C[n]_{p_t}^{p_b}$ is the cumulative conversion of APE into KE. Putting $l = 0$ in Eqs. (28) and (29) we recover Eqs. (5) and (6) integrated between two pressure surfaces.

3. Application to two GCMs

a. Presentation of the data and the models

We have analyzed two datasets produced with two spectral GCMs: the Atmospheric GCM for the Earth Simulator (AFES) and ECMWF's weather prediction model Integrated Forecast System (IFS). For a precise description of each simulations, see Hamilton et al. (2008) and ECMWF (2010), respectively. The two simulations and the two models are quite different. The AFES is a climate model using a spectral advection scheme. It has been run at high resolution for research purposes. The horizontal resolution is T639, which corresponds to a minimum wavelength of roughly 60 km. The model is formulated in sigma coordinates with 24 vertical levels from the ground to about 1 hPa leading to a vertical grid space corresponding to approximately 2 km in the high troposphere. Takahashi et al. (2006) and Hamilton et al. (2008) showed that the AFES reproduces many features of the atmospheric spectra, especially a realistic $k^{-5/3}$ power law at the mesoscales. For each truncation wavenumber l_T, the value of the horizontal hyperdiffusion coefficient κ_h was adjusted by trial and error to produce power-law spectra that agree with observations. However, for the runs at sufficiently large resolution (T639 and T1279) the existence of a distinct $k^{-5/3}$ mesoscale range was shown to be independent of the hyperdiffusion employed. Moreover, Takahashi et al. (2006) showed that the tuned horizontal hyperdiffusion coefficient scales with the truncation wavenumber as $\kappa_h \propto l_T^{-3.22}$. According to energy cascade phenomenology, this coefficient should only depend on the spectral flux through the inertial range Π, and the resolution scale so that the dissipation will take place at the smallest resolved scales and will be approximately equal to Π. Dimensional considerations then give $\kappa_h \simeq \Pi^{1/3} l_T^{-10/3}$. This good agreement between the theoretical and the empirically determined scaling laws indicates that the $k^{-5/3}$ spectra in the AFES models are produced by a downscale energy cascade (Hamilton et al. 2008). ECMWF IFS is a model developed and used for operational deterministic forecast. It uses a semi-Lagrangian advection scheme with a horizontal resolution T1279, which corresponds to a minimum wavelength of roughly 30 km. The model is formulated in hybrid coordinates with 91 vertical levels and a minimum pressure of 1 Pa. This leads to a vertical grid space corresponding to approximately 500 m in the high troposphere. A semi-implicit time scheme makes it possible to run this model with a much larger time step (600 s) than the one used for the AFES T639 model (100 s). The AFES and the ECMWF simulations correspond to June and December, respectively. We have averaged over 10 days

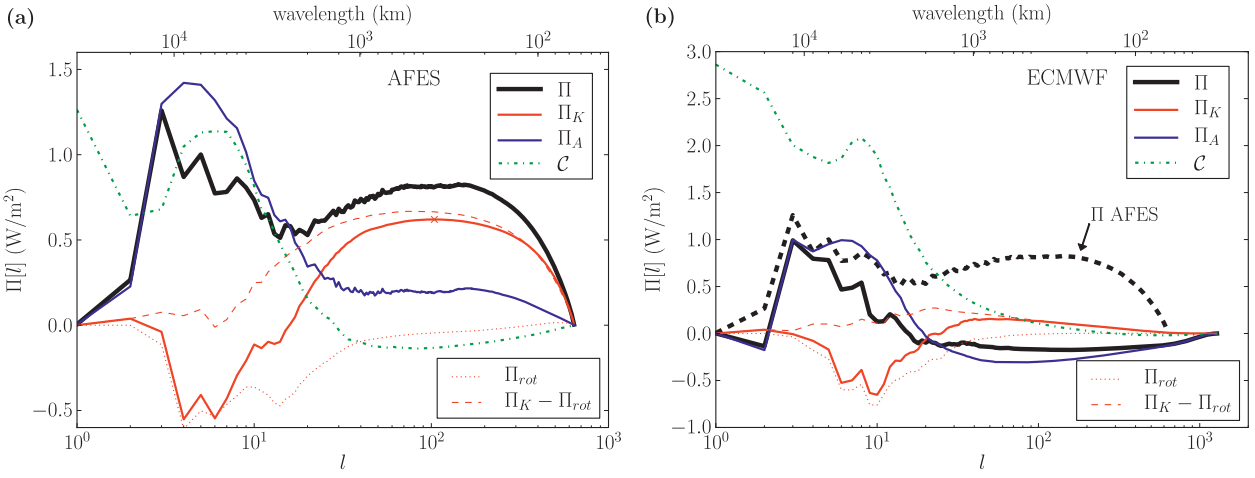

FIG. 1. Total, KE, and APE nonlinear spectral fluxes and cumulative conversion $\mathcal{C}[l]$ vs total wavenumber for (a) the AFES T639 simulation and (b) the ECMWF IFS T1279 simulation. The cross in (a) marks the maximum value of the KE nonlinear spectral flux $\tilde{\Pi}_K = \max(\Pi_K) = 0.62$ used for nondimensionalization of the spectra in Fig. 2. In (b), the black dashed line is the spectral flux $\Pi[l]$ for the AFES T639 simulation.

(40 times) for the AFES dataset and over 25 days (5 different times) for the ECMWF dataset. The time variations of the spectra and of the terms involved in the spectral energy budget are not very large, so that averages over such limited statistics represent the important features of the models, especially at the mesoscales for which a statistical convergence seems to be achieved. Other computations for the ECMWF model for August have shown that seasonality cannot explain the main differences between the models.

The AFES data are already linearly interpolated from the model levels and consist of the horizontal velocity, the pressure velocity, and the temperature at pressure levels. The geopotential is computed by integrating the hydrostatic relation from the ground. The ECMWF data are raw data from the model outputs. They contain the vorticity, the divergence, the pressure velocity, and the temperature at hybrid vertical levels. We compute horizontal velocity and the geopotential and then linearly interpolate the data at pressure levels. The interpolation method is thus the same for both models. Since we do not have access to the heating rate and to the total dissipative terms, the APE forcing $\mathcal{G}[l]_{p_t}^{p_b}$ and the dissipative terms $\mathcal{D}_K[l]_{p_t}^{p_b}$ and $\mathcal{D}_A[l]_{p_t}^{p_b}$ have not been computed. Since the surface fluxes are modeled in a GCM, we focus on the vertical flux at pressure levels not pierced by the topography. Finally, we have computed the terms $\mathcal{C}[l]_{p_t}^{p_b}$, $\Pi_K[l]_{p_t}^{p_b}$, $\Pi_A[l]_{p_t}^{p_b}$, and $\mathcal{L}[l]_{p_t}^{p_b}$ for all levels and the vertical fluxes $\mathcal{F}_{K\uparrow}[l](p)$ and $\mathcal{F}_{A\uparrow}[l](p)$ for pressure levels not pierced by the topography. The spectral flux arising from the Coriolis term $\mathcal{L}[l]_{p_t}^{p_b}$ is completely negligible at wavenumbers $l \gtrsim 10$, consistent with previous computations by Koshyk and Hamilton (2001). At larger scales, it is not negligible and is quite similar for both models. The Coriolis strength leads to a positive vertically integrated spectral flux on the order of 1 W m^{-2} from $l \simeq 2$ to $l \simeq 6$ with dominant contribution from the stratosphere. The linear flux $\mathcal{L}[l](p)$ is small in the troposphere for all wavenumbers. Since our main interest here is the dynamics of the mesoscales and for clarity, this spectral flux is not included in the figures.

b. *Vertically integrated spectral energy budget*

Figure 1a presents the globally integrated spectral fluxes and cumulative conversion for the AFES model. When vertically integrated over the total height of the atmosphere, these quantities are simply denoted $\Pi_K[l]$, $\Pi_A[l]$, and $\mathcal{C}[l]$ (i.e., without the top and bottom pressures in subscript and exponent). By construction, the fluxes are equal to zero at $l = l_{\max}$ and should also be equal to zero at $l = 0$, since they represent conservative processes. The total spectral flux (black thick line) is positive at all wavenumbers, which means that on average, the energy is transferred toward large wavenumbers. At leading order, energy is forced at the very large planetary scales and dissipated at smaller scales, and a substantial part is dissipated at the smallest scales simulated.

However, the total spectral flux has a somewhat intricate shape. It reaches a maximum equal to 1.3 W m^{-2} around $l = 4$, decreases to 0.55 W m^{-2} at $l \simeq 20$, and increases again to reach a plateau between $l \simeq 70$ and $l \simeq 200$ where $\Pi[l] \simeq 0.82$ W m^{-2} before dropping down to zero at the largest wavenumbers. At $l < 15$, the total flux is largely dominated by the APE spectral flux (blue line), which also increases abruptly around $l = 2$ and

decreases abruptly between $l = 6$ and $l = 20$. This indicates that there is a transfer of APE from wavelengths on the order of 10 000 km to wavelengths between 2000 and 5000 km. The strong decrease of $\Pi_A[l]$ is associated with a strong increase of the KE spectral flux (red line) and a strong decrease of the cumulative conversion (dashed–dotted line) from $\mathcal{C}[l] = 1.13$ to $-0.14\,\mathrm{W\,m^{-2}}$. The amount of energy that is converted from APE to KE in the wavenumber range $[l_1, l_2]$ is equal to $\Delta\mathcal{C} \equiv \mathcal{C}[l_1] - \mathcal{C}[l_2]$. (Note here the nonstandard definition of the difference operator Δ.) Therefore, the strong decrease of the cumulative conversion over the range of wavelengths between 1000 and 5000 km corresponds to a conversion of APE to KE of $\Delta\mathcal{C} \simeq 1.27\,\mathrm{W\,m^{-2}}$. This large conversion at the synoptic scales and the spectral transfer of APE from the planetary scales toward the synoptic scales are mainly due to the baroclinic instability. It is interesting to compare these results with the spectral energy budget of an equilibrated Eady flow (Molemaker and McWilliams 2010). The general picture is very similar with a dominance of the APE flux at large scales and a stronger KE flux at small scales. The increase of the total nonlinear flux at wavelengths between 700 and 2000 km indicates that there is a direct forcing of APE at these scales, most probably because of latent heat release organized at large scales. This interpretation is consistent with results by Hamilton et al. (2008), who reported spectral magnitude at the mesoscales much smaller for the dry dynamical core than for the full AFES.

As already shown, the KE is mainly forced (by a conversion of APE) over a range of wavelengths between 1000 and 5000 km. At larger scales, the KE spectral flux is negative and reaches a minimum value approximately equal to $-0.5\,\mathrm{W\,m^{-2}}$. A portion of the KE is transferred upscale, toward the planetary scales, and feeds the large-scale zonal winds. At smaller scales, the KE spectral flux reaches a plateau at $0.62\,\mathrm{W\,m^{-2}}$. This shows that a non-negligible portion of the KE cascades toward small scales at the mesoscales. The value $0.62\,\mathrm{W\,m^{-2}}$, which after conversion gives $6.1 \times 10^{-5}\,\mathrm{m^2\,s^{-3}}$, is consistent with previous estimations for the KE spectral flux and for the small-scale dissipation rate (Cho and Lindborg 2001). Remarkably, the cumulative conversion $\mathcal{C}[l]$ increases at the mesoscales (the local conversion is negative), showing that the conversion is from KE to APE. This demonstrates that the KE $k^{-5/3}$ spectrum is not produced by direct forcing of the KE. Note that this conversion from KE to APE is consistent with strongly stratified turbulence.

The nonlinear KE spectral flux computed only with the rotational flow Π_{rot} is plotted as a red dotted line. The interactions between the rotational modes conserve both KE and enstrophy ($|\nabla_h \wedge \mathbf{u}|^2/2$), exactly as in two-dimensional turbulence. Note that $\Pi_{\mathrm{rot}}[l]$ is the spectral flux computed when the framework based on the two-dimensional vorticity equation is adopted, as for example in Boer and Shepherd (1983). We see that these interactions are responsible for the upscale flux, which actually starts at wavelengths on the order of 2000 km. In contrast, the complementary flux, $\Pi_K[l] - \Pi_{\mathrm{rot}}[l]$ (red dashed line), is responsible for the downscale energy flux that starts at wavelengths on the order of 3000 km. Indeed, the downscale energy cascade is produced by interactions involving the divergent part of the velocity field (Molemaker et al. 2010; Deusebio et al. 2013).

As shown by Lambert (1984), the variations of the cumulative conversion at very small wavenumbers, $l < 8$, are due to the Hadley and Ferrel circulations. The decrease of $\mathcal{C}[l]$ at $l = 2$ corresponding to a conversion of APE to KE of approximately $0.6\,\mathrm{W\,m^{-2}}$ is mainly the signature of the Hadley cell. The increase of $\mathcal{C}[l]$ at $l = 4$ corresponding to a conversion of KE to APE of approximately $0.5\,\mathrm{W\,m^{-2}}$ is mainly the signature of the Ferrel cell. The conversion at $l = 2$ is weaker than previously computed by Lambert (1984). Further investigations are necessary to understand if this effect is due to averaging over an insufficient amount of data or if it is a robust aspect of the AFES.

Figure 1b presents the globally integrated spectral fluxes and cumulative conversion as in Fig. 1a, but for the ECMWF model. The planetary-scale features are overall quite similar to the results for the other model even though the conversion at wavenumbers smaller than 4 corresponding to the Hadley cell is much stronger ($\Delta\mathcal{C} \simeq 1\,\mathrm{W\,m^{-2}}$). The total conversion $\mathcal{C}[l = 0]$ is equal to $2.9\,\mathrm{W\,m^{-2}}$, consistent with results by Boer and Lambert (2008), who, averaging over a longer time period, computed a total conversion for the ECMWF model of $3.1\,\mathrm{W\,m^{-2}}$. The baroclinic instability leads to large-scale positive APE flux and strong conversion at the synoptic scales $\Delta\mathcal{C} \simeq 1.5\,\mathrm{W\,m^{-2}}$. However, the KE flux increases much less than for the AFES, indicating that there is strong dissipation at wavelengths on the order of 2000 km. The total spectral flux for the AFES is also plotted in dashed black line for comparison. The total flux for the ECMWF model is slightly smaller than for the AFES at the synoptic scales and is negative and very small at the mesoscales. This is related to the weakness of the downscale mesoscale KE cascade ($\Pi_K[l] \simeq 0.15\,\mathrm{W\,m^{-2}}$) and to the fact that the APE flux is negative ($\Pi_A[l] \simeq -0.3\,\mathrm{W\,m^{-2}}$). This unexpected result could be due to direct forcing of APE by release of latent heat at the smallest resolved scales on the order of 50 km. This interpretation is consistent with the sign of the local

TABLE 1. Quantitative energy budget ($W\,m^{-2}$) for the range of wavenumbers from $l_1 = 12$ to $l_2 = 40$—that is, for wavelengths between 1000 and 3200 km corresponding approximately to the synoptic scales, for the AFES and the ECMWF models. The quantities $\Delta\mathcal{C}$, $\Delta\Pi_K$, $\Delta\Pi_A$, and $\Delta\Pi$ are directly obtained from Fig. 1. The other quantities are evaluated using Eqs. (30)–(32).

	AFES	ECMWF
$\Delta\mathcal{C}$	0.73	1.23
$\Delta\Pi_K$	−0.63	−0.51
$\Delta\Pi_A$	0.54	1.83
$\Delta\Pi$	−0.09	0.32
$\Delta\mathcal{D}_K$	0.10	0.72
$\Delta\mathcal{G} - \Delta\mathcal{D}_A$	0.19	0.41
$\Delta\mathcal{G} - \Delta\mathcal{D}$	0.09	−0.31

TABLE 2. As in Table 1, but for l_2 equal to the largest wavelength resolved by the model and for $l_1 = 100$, which corresponds to a wavenumber of approximately 400 km. This range of wavenumbers includes the mesoscales and the smallest length scales resolved by the models.

	AFES	ECMWF
$\Delta\mathcal{C}$	−0.13	0.11
$\Delta\Pi_K$	0.62	0.13
$\Delta\Pi_A$	0.19	−0.30
$\Delta\Pi$	0.81	−0.17
$\Delta\mathcal{D}_K$	0.48	0.24
$\Delta\mathcal{G} - \Delta\mathcal{D}_A$	−0.32	0.41
$\Delta\mathcal{G} - \Delta\mathcal{D}$	−0.81	0.17

conversion at the mesoscales, from APE to KE, in contrast to the case of AFES.

We shall now present a quantitative comparison between the two models. In a stationary state, the amount of KE that is dissipated in a wavenumber range $[l_1, l_2]$ can be estimated as

$$\Delta\mathcal{D}_K \simeq \Delta\mathcal{C} + \Delta\Pi_K, \tag{30}$$

where $\Delta\mathcal{C} \equiv \mathcal{C}[l_1] - \mathcal{C}[l_2]$ is the amount of APE converted to KE in the range $[l_1, l_2]$ and $\Delta\Pi_K \equiv \Pi_K[l_1] - \Pi_K[l_2]$ is the net amount of energy going into the range $[l_1, l_2]$ by the nonlinear fluxes at l_1 and l_2. The effective forcing of APE can be evaluated in the corresponding way as

$$\Delta\mathcal{G} - \Delta\mathcal{D}_A \simeq \Delta\mathcal{C} - \Delta\Pi_A. \tag{31}$$

Finally, the effective total forcing can be evaluated as

$$\Delta\mathcal{G} - \Delta\mathcal{D} \simeq -\Delta\Pi, \tag{32}$$

where $\mathcal{D}[l] = \mathcal{D}_K[l] + \mathcal{D}_A[l]$ is the total energy dissipation and $\Pi[l]$ the total energy spectral flux. Any increase (decrease) of the total energy flux implies a net positive (negative) forcing of the total energy.

Table 1 summarizes the main differences between the two models in terms of the energy budget of the synoptic scales, with $l_1 = 12$ and $l_2 = 40$ corresponding to wavelengths between 1000 and 3200 km. The most important difference for these scales is $\Delta\mathcal{D}_K$, which is equal to $0.10\,W\,m^{-2}$ for the AFES model and to $0.72\,W\,m^{-2}$ for the ECMWF model. As already mentioned, the ECMWF model is very dissipative at the synoptic scales. We have verified that a large part of this synoptic-scale dissipation takes place in the free atmosphere (i.e., far from the surface). This unexpected and anomalous result could explain the lack of downscale energy cascade at the mesoscales observed for this model. For both models, there is a net positive effective forcing of APE, $\Delta\mathcal{G} - \Delta\mathcal{D}_A$, which is the signature of release of latent heat organized at the synoptic scales. For the AFES, this release of latent heat is larger than the KE dissipation ($\Delta\mathcal{G} - \Delta\mathcal{D} > 0$), which leads to an increase of $\Pi[l]$. In contrast, for the ECMWF model the KE dissipation is larger than the effective forcing of APE ($\Delta\mathcal{G} - \Delta\mathcal{D} < 0$) so that the total flux decreases to approximately zero at $l = 1000$.

Table 2 presents a similar energy budget as Table 1, but for $l > 100$ (i.e., for the mesoscales and the smallest length scales resolved by the models). Only a small fraction ($0.24\,W\,m^{-2}$) of the total KE dissipation ($\mathcal{C}[0] = 2.9\,W\,m^{-2}$) takes place at these scales for the ECMWF model, whereas these scales account for a significant part of the KE dissipation for the AFES. Remarkably, $\Delta\mathcal{G} - \Delta\mathcal{D}_A$ is negative for the AFES ($-0.32\,W\,m^{-2}$) and positive for the ECMWF model ($0.41\,W\,m^{-2}$). In this model, the APE and KE are directly forced at small scales by latent heat release and conversion characterized by a weak spatial coherence.

c. Vertically integrated nondimensional spectra

If it is assumed that the $l^{-5/3}$ range of the kinetic energy spectrum is of a similar form as the Kolmogorov spectrum of isotropic turbulence, then $E_K \propto \Pi_K^{2/3} l^{-5/3}$. If it is further assumed that the only other parameters that determine the spectrum are the radius of Earth and the total mass per unit area, which is equal to $\langle p_s \rangle / g$, then dimensional considerations give

$$E_K[l] = C(\langle p_s \rangle / g)^{1/3} (a\Pi_K)^{2/3} l^{-5/3}, \tag{33}$$

where C is a constant supposedly on the order of unity. In the following, we choose as the typical KE flux the maximum of the KE flux: $\tilde{\Pi}_K = \max(\Pi_K) = 0.62$. (This value is marked by a cross in Fig. 1a.) In Fig. 2a the nondimensional compensated spectra $E[l] l^{5/3} (\langle p_s \rangle / g)^{-1/3} (a\tilde{\Pi}_K)^{-2/3}$ for the AFES model are plotted as a function of the total wavenumber. At $l = 1$, the APE spectrum (blue line) is

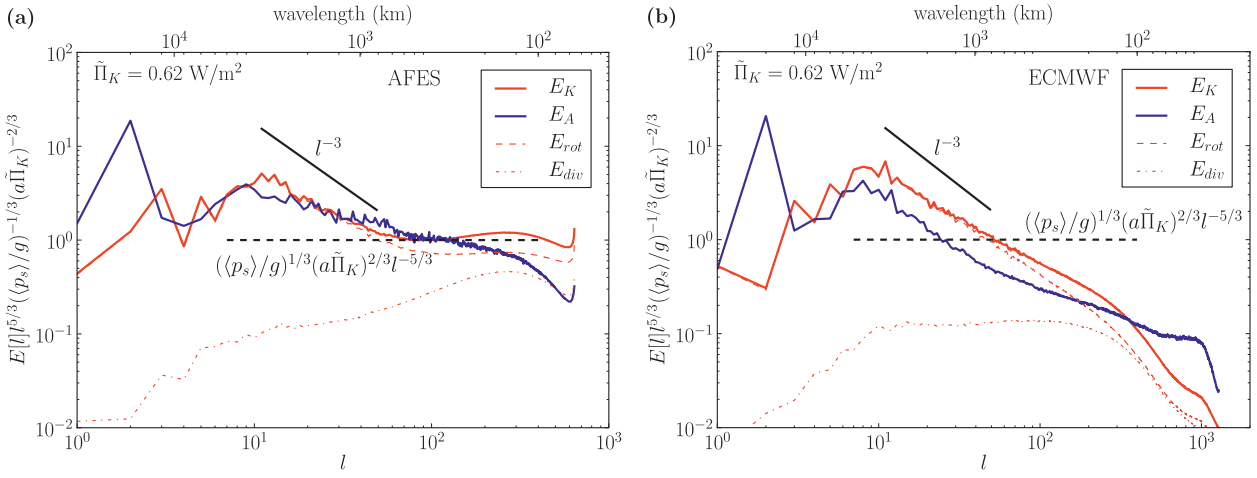

FIG. 2. Nondimensional compensated spectra vs total wavenumber for (a) the AFES T639 simulation and (b) the ECMWF IFS T1279 simulation. The black dashed line represents the prediction in Eq. (33) with $\tilde{\Pi}_K = 0.62$ (value marked by a cross in Fig. 1a). The continuous straight line indicates the l^{-3} power law.

much larger than the KE spectrum (red line), as predicted by Lorenz (1955). This leads to a ratio mean APE over mean KE approximately equal to 3. However, for other wavenumbers (except at the largest ones), both spectra are of the same order of magnitude. At the synoptic scales, the KE spectrum is quite steep. It shallows at the mesoscales and presents a flat plateau corresponding to an $l^{-5/3}$ inertial range from 650 km up to the large-wavenumber dissipative range. Remarkably, the constant C in Eq. (33) is very close to unity, which indicates that the $l^{-5/3}$ mesoscale range may be explained in a similar way as Kolmogorov (1941) explained the $k^{-5/3}$ range of isotropic turbulence. At wavelengths between 700 and 2000 km, the APE spectrum (blue line) is equal to or larger than the KE spectrum and there are fluctuations resembling noise. However, the fluctuations do not seem related to lack of statistics. They could be due to the direct forcing of APE at these scales (see Fig. 1a).

In Fig. 2 are also plotted the rotational spectrum $E_{\rm rot}[l]$ and the divergent spectrum $E_{\rm div}[l]$ computed as in Eq. (13). At large scales, $E_{\rm rot}[l]$ (dashed red line) totally dominates over $E_{\rm div}[l]$ (dashed–dotted red line). Remarkably, the compensated divergence spectrum increases with l, meaning that $E_{\rm div}[l]$ is shallower than an $l^{-5/3}$ power law. Such very shallow divergent spectra were also obtained by simulations of strongly stratified and strongly rotating turbulence forced in geostrophic modes (Deusebio et al. 2013) and of strongly stratified turbulence forced with rotational modes (Augier et al. 2013, manuscript submitted to *J. Fluid Mech.*). However, other simulations with higher resolution would be necessary in order to check whether the divergent spectra are sensitive to model parameterizations and resolution. At the mesoscales, both spectra are of the same order of magnitude even though $E_{\rm rot}[l]$ is larger than $E_{\rm div}[l]$.

Figure 2b shows the nondimensional compensated spectra for the ECMWF model (we use the same value as for the AFES of $\tilde{\Pi}_K$ in order to allow an easier comparison between both models). The planetary-scale features are quite similar to the AFES. At the synoptic scales, the ratio $E_K[l]/E_A[l]$ is approximately equal to 2, indicating that the energy is partitioned equally between the two components of KE and the APE, as predicted by Charney (1971). In contrast to the KE spectrum, the APE spectrum becomes shallower at high wavenumbers. This is probably due to direct forcing of APE at the mesoscales. Interestingly, the compensated divergent spectrum is flat, which means that it follows an $l^{-5/3}$ power law. However, its magnitude is very small so that the vertically integrated KE spectrum at the mesoscales is nearly not affected. It is interesting to note the similarity with the $k^{-5/3}$ divergent spectra obtained by Waite and Snyder (2009) simulating a baroclinic life cycle.

d. Vertical decomposition and vertical energy fluxes

Figure 3 presents the spectral fluxes and the cumulative conversion integrated over two different layers corresponding approximately to the upper troposphere (Figs. 3a,b) and the stratosphere (Figs. 3c,d). Figures 3a and 3c correspond to the AFES T639 simulation and Figs. 3b and 3d to the ECMWF IFS T1279 simulation. Figure 3 also presents the cumulative total vertical fluxes, $\mathcal{F}_\uparrow[l](p_b)$ at the bottom and $\mathcal{F}_\uparrow[l](p_t)$ at the top of the layer (magenta dashed and dashed–dotted lines, respectively). The balance between these two inward and outward terms, $\Delta_{p_t}^{p_b}\mathcal{F}_\uparrow[l] = \mathcal{F}_\uparrow[l](p_b) - \mathcal{F}_\uparrow[l](p_t)$, is plotted in magenta as a continuous line.

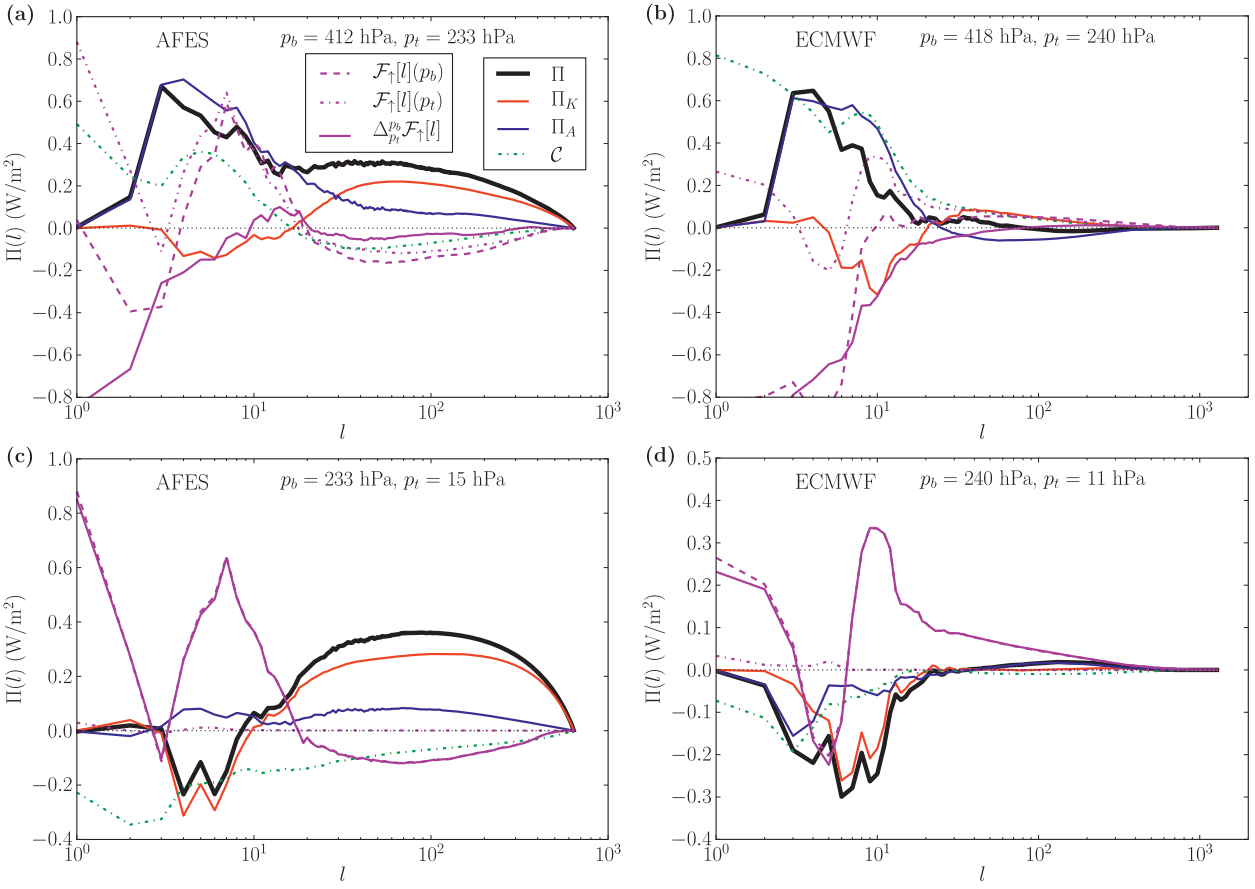

FIG. 3. As in Fig. 1, but integrated over layers corresponding approximately to (a),(b) the stratosphere and (c),(d) the upper troposphere. Panels correspond to (a),(c) the AFES T639 simulation and (b),(d) the ECMWF IFS T1279 simulation. The legend is given in (a) and $\Delta_{p_t}^{p_b}\mathcal{F}_\uparrow[l] = \mathcal{F}_\uparrow[l](p_b) - \mathcal{F}_\uparrow[l](p_t)$ is the cumulative inward vertical flux.

For the AFES simulation, the spectral fluxes and the cumulative conversion integrated over the upper troposphere (Fig. 3a) present roughly the same features as the globally integrated terms shown in Fig. 1a. The KE flux in the upper troposphere accounts for approximately one-third of the globally integrated KE spectral flux. The cumulative vertical flux $\Delta_{p_t}^{p_b}\mathcal{F}_\uparrow[l]$ is relatively small at the mesoscales and at the synoptic scales, indicating that at leading order, the energy budget in this layer and at these scales is dominated by the spectral fluxes rather than by the vertical fluxes. However, at the top and the bottom of the layer, there are large vertical fluxes that are approximately equal. These fluxes through the upper troposphere (upward at wavenumbers $7 \le l \le 20$ and downward at wavenumbers $3 \le l \le 6$) account for exchanges of energy between the lower troposphere and the stratosphere. At wavenumbers $1 \le l \le 2$, $\mathcal{F}_\uparrow[l](p_t)$ decreases from 0.8 to 0 W m^{-2}, indicating a strong upward vertical flux at $p_t = 233$ hPa. Since the vertical flux at the bottom layer is small at these wavenumbers, the layer loses energy. The wavenumber ranges of the upward and downward fluxes at the planetary scales nearly coincide with the wavenumber ranges of the conversion due to the Hadley and Ferrel cells, which seems to indicate that these vertical fluxes are related to the large-scale cells. In contrast, the upward flux at the synoptic scales indicates the presence of upward-propagating planetary waves. At $l > 70$, $\mathcal{F}_\uparrow[l](p_b)$ and $\mathcal{F}_\uparrow[l](p_t)$ increase, meaning that there is a downward vertical flux at these scales. This shows that in the AFES, the mesoscales of the upper troposphere are not directly forced by upward-propagating gravity waves, as was the case in the simulation by Koshyk and Hamilton (2001) using the SKYHI model.

Figure 3b presents the same quantities as Fig. 3a, also integrated over the upper troposphere, but for the ECMWF model. Comparing Figs. 3a and 3b, we see the same differences as we saw between Figs. 1a and 1b. The vertical fluxes are also quite different from the AFES with small upward fluxes at the mesoscales and a smaller magnitude of the variations of the cumulative fluxes at large scales.

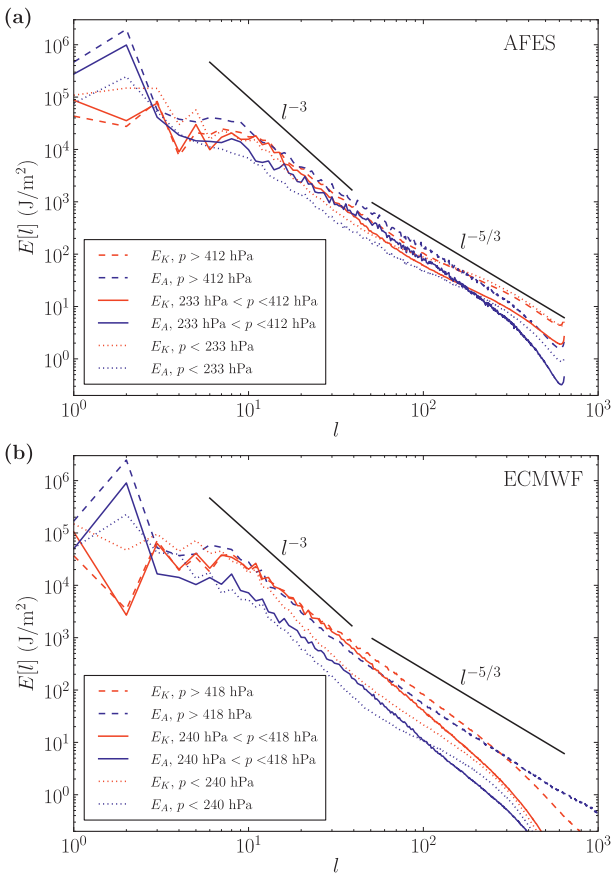

FIG. 4. KE and APE spectra integrated over three layers corresponding approximately to the lower troposphere, the upper troposphere, and the upper atmosphere. The straight black lines indicate the l^{-3} and $l^{-5/3}$ dependencies as guides for the eye. Note that the axes and the straight lines are exactly the same in both panels.

Figure 3c shows the same quantities as Fig. 3a, also for the AFES, but integrated over the stratosphere. At the large scales, the spectral fluxes and the cumulative conversion are quite different from the terms integrated over the height of the atmosphere and over the upper troposphere. The APE flux has no large peak at $l \simeq 4$ and there is a conversion from KE to APE at synoptic scales rather than the other way around, as in the upper troposphere. On the other hand, there is a strong upward energy flux at large scales from the bottom layer at $p_b =$ 233 hPa while the corresponding flux at the top layer at $p_t = 15$ hPa is very small. Thus, the stratosphere is not directly forced by baroclinic instability, but by an energy flux from the troposphere, owing to upward-propagating planetary waves and possibly also the effects of the Hadley and the Ferrel cells (see Fig. 3a). At the mesoscales, there is a conversion of KE into APE and a strong downscale cascade of KE and APE, accounting for approximately half the globally integrated flux. At $l > 80$, $\Delta_{p_t}^{p_b}\mathcal{F}_\uparrow[l] \simeq \mathcal{F}_\uparrow[l](p_b)$ increases, meaning that the stratosphere loses energy by a downward flux through the tropopause.

Figure 3d presents the same quantities as Fig. 3c, also integrated over the stratosphere, but for the ECMWF model. Note that the vertical axis is different from Fig. 3c. In contrast to the AFES, the downscale energy cascade is very small and the stratospheric mesoscales are directly forced by an upward energy flux.

Figure 4 presents the KE and APE spectra integrated over three layers corresponding approximately to the lower troposphere, the upper troposphere, and the upper atmosphere for the AFES (Fig. 4a) and the ECMWF model (Fig. 4b). Note that the axes and the straight lines are exactly the same in both figures. At the large scales the spectra for both models are similar, but at the mesoscales the spectral magnitude of the ECMWF is much smaller than the magnitude of the AFES. Spectra integrated over the different layers lie closer to each other for the AFES than for the ECMWF. For the AFES the KE spectra have similar shapes at different layers, whereas for the ECMWF model, they are quite different with a shallowing at the mesoscales only in the stratosphere (blue and red dotted lines) as reported by Burgess et al. (2013). However, these shallow spectra are much smaller in magnitude than the corresponding spectra from the AFES model (more than one order of magnitude smaller at $l \simeq 100$). From Fig. 3d it is quite clear that the shallowing of the stratospheric spectra of the ECMWF model is not caused by an energy cascade, but rather by gravity waves propagating from the troposphere. The integrated spectra of the ECMWF model (Fig. 2b) is dominated by the contribution from the troposphere. In the lower troposphere, the APE spectrum presents an $l^{-5/3}$ dependency and is larger than the KE spectrum at large wavenumbers. However, this cannot be explained by a downscale energy cascade since the APE spectral flux is small and negative. These differences between the APE and the KE spectra could be due to a damping of the KE and to a direct diabatic forcing of the APE at the very large wavenumbers ($l \sim 1000$). For the AFES model (Fig. 4a), the spiky irregular shape observed at the synoptic scales for the globally integrated APE spectrum (Fig. 2a) is also observed for the tropospheric APE spectra but not for the stratospheric APE spectrum. This could indicate that this effect is related to the topography. However, the spikes are present in not only the lower- but also the upper-tropospheric spectra whereas the upper troposphere is not pierced by the topography. Moreover, the vertical fluxes at $p = 412$ hPa are rather regular. Therefore, the spiky irregular shape of the APE spectra seems to be due to processes happening in the troposphere and not only at the surface. The release of

latent heat organized at the synoptic scales could be an explanation.

4. Conclusions

A new formulation of the spectral energy budget has been presented and applied to study the results of two different GCMs. In contrast to previous formulations, both KE and APE are considered and the topography is taken into account. Moreover, the advection terms are exactly separated into spectral transfer and vertical flux and the pressure term is exactly separated into adiabatic conversion and vertical flux.

The spectral fluxes show that the AFES, which produces realistic $k^{-5/3}$ KE spectra at the mesoscales, simulates a strong downscale energy cascade of $\Pi[l] = 0.8\,\mathrm{W\,m^{-2}}$. The vertical fluxes for the upper troposphere show that the mesoscales are not directly energized by gravity waves propagating from the ground. Moreover, the spectra collapse on the prediction based on the existence of the cascade, indicating that the mesoscale $k^{-5/3}$ power law is due to the downscale energy cascade. In contrast, neither the $k^{-5/3}$ KE spectrum nor the downscale energy cascade is produced by the ECMWF model. The analysis of the spectra and their tendencies integrated over different layers reveals that in the ECMWF, the stratospheric mesoscales are directly forced by gravity waves propagating from the troposphere. In contrast, the stratospheric spectra of the AFES are forced by the downscale energy cascade and at the mesoscales, gravity waves produced in the stratosphere propagate to the troposphere.

These results show that our spectral energy budget formulation is a convenient tool to investigate the issue of the mesoscale dynamics and its simulation by GCMs. In particular, we have shown that the flux computed only with the rotational part of the velocity field Π_{rot} [as, e.g., in Fjørtoft (1953) and Boer and Shepherd (1983)] accounts only for the upscale KE flux. Since the downscale energy cascade is produced by interactions involving the divergent part of the velocity field (Vallgren et al. 2011; Deusebio et al. 2013; Molemaker et al. 2010), one must consider the nonlinear transfers computed with the total advection term. To do this in a consistent way, the advection terms in the spectral energy budget have to be split as shown in section 2.

Our results raise many interesting questions. In particular, we have shown that the two studied models simulate very different dynamics at the mesoscales. The AFES model reproduces a downscale energy cascade at the mesoscales, whereas such a cascade is absent in the ECMWF model. One important difference between the two models is the vertical resolution. The vertical grid space in the high troposphere in approximately 500 m for the ECMWF model and 2 km for the AFES model. A coarser resolution should be a drawback for simulating the mesoscale dynamics, both gravity waves and strongly stratified turbulence. The ECMWF model can simulate gravity waves with smaller vertical resolution than those simulated by the AFES model. Stratified turbulence is very demanding in terms of vertical resolution, since it is necessary to resolve the buoyancy length scale, $L_b \sim U/N$, which is the characteristic vertical length scale of horizontal layers (Waite and Bartello 2004; Lindborg 2006; Waite 2011). Here, U is the characteristic velocity of the horizontal wind and N is the Brunt–Väisälä frequency. Since L_b is on the order of 1 km in the atmosphere, none of the models really resolves this length scale. The question is, then, how is it possible that either of these two models is able to simulate a downscale energy cascade? Our tentative answer to this question is that vertical resolution does not seem to be very critical in order to reproduce a downscale energy cascade, because such a cascade seems to be a very general property of rotating and stratified hydrodynamic systems that are not too close to the quasigeostrophic regime. That a downscale energy cascade emerges in such systems has been demonstrated in recent simulations (Molemaker et al. 2010) that do not have extremely fine vertical resolution. Dynamically, the downscale cascade is characterized by the importance of the interactions involving ageostrophic modes. This raises the question of how ageostrophic motions at scales on the order of thousands of kilometers are produced from geostrophic motions at large scales. In particular, the baroclinic instability does not produce ageostrophic motions. Our results indicate that other ageostrophic instabilities are active and very important in the AFES model.

In subsection 3b, we have discussed the energy budget of the synoptic scales (see Table 1). We have shown that the ECMWF model is very dissipative, even at these very large scales. In the atmosphere, the dissipation takes place at scales on the order of 1 cm or smaller. In a GCM, dissipation—namely, loss of energy at resolved scales—has to correspond to physical processes transferring energy to unresolved scales. It seems unlikely that physical processes could account for such large highly nonlocal transfer from the synoptic scales to the unresolved scales, which are relatively small for the ECMWF T1279L91 model. This indicates that the synoptic-scale dissipation for the ECMWF model is too large. Since energy is removed at the synoptic scales, it is not available to feed the downscale energy cascade. Our interpretation of the data analysis is that the ECMWF model does not simulate the downscale cascade at the mesoscales because of an excessive dissipation

at the synoptic scales. If this interpretation is correct, a decrease of the dissipation at the synoptic scales would have strong consequences in terms of the mesoscale dynamics. Thus, it would be important to understand why the ECMWF model is so dissipative at the synoptic scales. One explanation could be numerical dissipation related to the semi-Lagrangian semi-implicit scheme. However, it seems unlikely that the numerical scheme could account for such large dissipation at scales approximately 200 times larger than the typical horizontal grid scale, which is equal to 16 km. Therefore, it would be interesting to explicitly compute the dissipation spectrum of all nonconservative terms related to, for example, the turbulent scheme and the wave drag.

Future investigations could also compare different models varying the resolution, the convection schemes, the advection scheme, and the turbulent models. It would be desirable to analyze simulations over long periods to obtain better statistical convergence at large scales. It could be informative to analyze idealized simulations using dry dynamical core and/or aquaplanet versions of the models with variation of physical parameters such as the rotation rate and the large-scale forcing. Other interesting aspects for future work are the consideration of the effects of the water content and the adaptation of the formulation for nonhydrostatic simulations.

Acknowledgments. We wish to thank Kevin Hamilton and Nils Wedi for providing the data. We thank Kevin Hamilton for showing nice hospitality in Hawaii, Erland Källén and Nils Wedi for inviting us to ECMWF where we had interesting discussions, and Nathanael Schaeffer for providing his library for spherical harmonic transform SHTns (Schaeffer 2013). We also thank two anonymous reviewers for useful comments.

APPENDIX A

Technical Details on Topography in p Coordinates

Following Boer (1982), the equations are extended over a domain including subterranean pressure levels. For any function $f(\mathbf{x}_h, p)$ whose values below the surface have been obtained by interpolation, we define a corresponding function $\tilde{f}(\mathbf{x}_h, p) = \beta(\mathbf{x}_h, p) f(\mathbf{x}_h, p)$, where $\beta(\mathbf{x}_h, p) = \mathrm{H}[p_s(\mathbf{x}_h) - p]$ and H is the Heaviside function. In the extended domain, the boundary condition at the earth surface is expressed as $\mathrm{D}_t\beta = 0$, with $\mathrm{D}_t = \partial_t + \mathbf{v}\cdot\boldsymbol{\nabla}$. Using the chain rules $\partial_t\beta = \delta\partial_t p_s$, $\boldsymbol{\nabla}_h\beta = \delta\boldsymbol{\nabla}_h p_s$, and $\partial_p\beta = -\delta$, we recover the classical boundary condition for the atmospheric domain in pressure coordinates: $\mathrm{D}_t\beta = \delta(\partial_t p_s + \mathbf{u}\cdot\boldsymbol{\nabla}_h p_s - \omega_s) = 0$, where $\delta = \delta(p_s - p)$ is the Dirac distribution with impulse at the surface. Note that taking into account the topography has of course no influence for the high troposphere and the stratosphere. However, the increase of the accuracy is important for the lower troposphere, especially through the computation of the representative mean temperature without using interpolated subterranean data.

For each pressure level, even those pierced by the topography, the spectral energy functions are defined as

$$E_K^{lm}(p) = \frac{(\tilde{\mathbf{u}}, \tilde{\mathbf{u}})_{lm}}{2} \quad \text{and} \quad E_A^{lm}(p) = \gamma(p)\frac{|\tilde{\theta}'_{lm}(p)|^2}{2}.$$

The spectral energy budget is derived as in section 2—that is, using the relations $\partial_t E_K^{lm}(p) = (\tilde{\mathbf{u}}, \partial_t\tilde{\mathbf{u}})_{lm}$ and $\partial_t E_A^{lm}(p) = \gamma(p)(\tilde{\theta}', \partial_t\tilde{\theta}')_{lm}$. For levels pierced by the topography, a surface term arises from the pressure term $(\tilde{\mathbf{u}}, \beta\boldsymbol{\nabla}_h\Phi)_{lm}$ and can be expressed as

$$S^{lm}(p) = -(\tilde{\omega}, \delta\Phi_s)_{lm} - (\delta\partial_t p_s, \tilde{\Phi})_{lm} + (\tilde{\mathbf{u}}, \delta\Phi_s\boldsymbol{\nabla}_h p_s)_{lm}. \tag{A1}$$

The sum over all spherical harmonics of $S^{lm}(p)$ is equal to the surface term $S(p)$ in Eq. (5). However, the term $S^{lm}(p)$ is difficult to evaluate and has not been computed.

The expressions of the other terms are very similar as those derived in section 2. The nonlinear transfers can be written as

$$T_K^{lm}(p) = -(\tilde{\mathbf{u}}, \mathbf{u}\cdot\boldsymbol{\nabla}_h\tilde{\mathbf{u}} + d\tilde{\mathbf{u}}/2)_{lm} + [(\partial_p\tilde{\mathbf{u}}, \omega\tilde{\mathbf{u}})_{lm} - (\tilde{\mathbf{u}}, \omega\partial_p\tilde{\mathbf{u}})_{lm}]/2, \tag{A2}$$

$$T_A^{lm}(p) = -\gamma(\tilde{\theta}', \mathbf{u}\cdot\boldsymbol{\nabla}_h\tilde{\theta}' + d\tilde{\theta}'/2)_{lm} + \gamma[(\partial_p\tilde{\theta}', \omega\tilde{\theta}')_{lm} - (\tilde{\theta}', \omega\partial_p\tilde{\theta}')_{lm}]/2. \tag{A3}$$

The linear transfer arising from the Coriolis strength is

$$L^{lm}(p) = f_0\{[\breve{\psi}, \sin\varphi\,\mathrm{div}_h(\tilde{\mathbf{u}}) + \cos\varphi\,\partial_\varphi\breve{\chi}]_{lm} + [\breve{\chi}, \sin\varphi\,\mathrm{rot}_h(\tilde{\mathbf{u}}) - \cos\varphi\,\partial_\varphi\breve{\psi}]_{lm}\}, \tag{A4}$$

where $\breve{\psi}$ and $\breve{\chi}$ are the streamfunction and velocity potential computed from $\tilde{\mathbf{u}}$. The diabatic term, the conversion term, and the diffusion terms are

$$G^{lm}(p) = \gamma(\tilde{\theta}', \tilde{Q}'_\theta)_{lm}, \tag{A5}$$

$$C^{lm}(p) = -(\tilde{\omega}, \tilde{\alpha})_{lm}, \tag{A6}$$

$$D_K^{lm}(p) = -[\tilde{\mathbf{u}}, \beta\mathrm{D}_{\mathbf{u}}(\mathbf{u})]_{lm}, \quad \text{and} \tag{A7}$$

$$D_A^{lm}(p) = -\gamma[\tilde{\theta}', \beta\mathrm{D}_\theta(\theta)]_{lm}. \tag{A8}$$

The vertical fluxes and the nonconservative term can be computed as

$$F^{lm}_{K\uparrow}(p) = -(\tilde{\omega}, \tilde{\Phi})_{lm} - (\tilde{\mathbf{u}}, \omega\tilde{\mathbf{u}})_{lm}/2, \quad \text{(A9)}$$

$$F^{lm}_{A\uparrow}(p) = -\gamma(\tilde{\theta}', \omega\tilde{\theta}')_{lm}/2, \quad \text{and} \quad \text{(A10)}$$

$$J^{lm}(p) = -(\partial_p \log\gamma)F^{lm}_{A\uparrow}(p). \quad \text{(A11)}$$

In practice, computing the spherical harmonics transform of $\tilde{\mathbf{u}} = \beta\mathbf{u}$ is not numerically feasible at pressure levels pierced by the topography (i.e., where β is equal to 1 or 0). We must use a modified smooth β. Moreover, the spherical harmonic transform of $\tilde{\mathbf{u}} = \beta\mathbf{u}$ should not reflect the spectral content of the topography rather than that of $\mathbf{u}$. Therefore, it is convenient to use an alternative β computed with a time-averaged pressure surface $\overline{p_s}(\mathbf{x}_h)$ (Boer 1982). A smooth low-pass filter with a cutoff total wavenumber equal to 40 is then applied to this function $\mathrm{H}[\overline{p_s}(\mathbf{x}_h) - p]$. As a consequence, a large part of the interpolated subterranean data (mainly under the large topographic highs—i.e., Antarctic continent and Himalaya and Andean mountain ranges) are not used in the calculations, but the spectral quantities at relatively high wavenumbers are not affected by the high wavenumber content of the topography.

APPENDIX B

Total Energy Conservation and APE

In this appendix, we investigate the meaning of the surface term appearing in Eq. (5) and show how Eqs. (5) and (6) can be related to the total energy conservation. Neglecting all diabatic processes, it is straightforward to derive the local conservation equation

$$\mathrm{D}_t(E_K + H) = -\nabla\cdot(\mathbf{v}\Phi), \quad \text{(B1)}$$

with $E_K(\mathbf{x}_h, p) = |\mathbf{u}|^2/2$. By computing $\mathrm{D}_t[\beta(E_K + H)]$, we obtain an equation that is valid over a domain including subterranean pressure levels

$$\mathrm{D}_t(\tilde{E}_K + \tilde{H}) = -\beta\nabla\cdot(\mathbf{v}\Phi) = -\nabla\cdot(\mathbf{v}\tilde{\Phi}) + \Phi\mathbf{v}\cdot\nabla\beta. \quad \text{(B2)}$$

Taking the horizontal mean and integrating over pressure gives

$$\partial_t\int_0^\infty \langle\tilde{E}_K + \tilde{H}\rangle\, dp/g = -\partial_t\langle\Phi_s p_s\rangle/g, \quad \text{(B3)}$$

where we have used the relations $\Phi\mathbf{v}\cdot\nabla\beta = -\Phi\partial_t\beta = -\delta\Phi_s\partial_t p_s$ and the fact that $\Phi_s(\mathbf{x}_h)$ is not a function of time.

Using the hydrostatic equation, it can be shown that $E_I + \Phi = H + \partial_p(p\Phi)$, which, after integration, gives

$$\partial_t\langle\Phi_s p_s\rangle/g = \partial_t\int_0^\infty \langle\tilde{E}_I + \tilde{\Phi} - \tilde{H}\rangle\, dp/g, \quad \text{(B4)}$$

where E_I is the internal energy per unit mass. Substituting this result into Eq. (B3) finally gives the total energy conservation equation

$$\partial_t\int_0^\infty \langle\tilde{E}_K + \tilde{E}_I + \tilde{\Phi}\rangle\, dp/g = 0. \quad \text{(B5)}$$

Note that Eqs. (B3) and (B4) can be rewritten as

$$\partial_t\int_0^\infty \langle\tilde{E}_K\rangle\, dp/g = \int_0^\infty C(p)\, dp/g - \partial_t\langle\Phi_s p_s\rangle/g, \quad \text{(B6)}$$

$$\partial_t\int_0^\infty \langle\tilde{E}_I + \tilde{\Phi}\rangle\, dp/g = -\int_0^\infty C(p)\, dp/g + \partial_t\langle\Phi_s p_s\rangle/g, \quad \text{(B7)}$$

which shows that the term $\partial_t\langle\Phi_s p_s\rangle/g$ can be interpreted as a conversion of E_K into $E_I + \Phi$. Using the hydrostatic equation, we find that $\langle\Phi_s p_s\rangle/g = \langle\Phi_s\rho_A\rangle$, where $\rho_A(\mathbf{x}_h, t)$ is the mass per unit area of the total depth of the atmosphere. Thus, $\langle\Phi_s p_s\rangle/g$ may be interpreted as the mean potential energy per unit area of an atmosphere where the center of mass of each air column has been moved to the ground. This quantity can change only if the density distribution is changed with respect to topography, so that high- or low-density air on average is moved to high- or low-topography regions.

The sum of Eqs. (5) and (6) integrated over pressure is

$$\partial_t\int_0^\infty \langle\tilde{E}_K + \tilde{E}_A\rangle\, dp/g = \int_0^\infty [S(p) + J(p)]\, dp/g,$$
$$= -\partial_t\langle\Phi_s p_s\rangle/g + \int_0^\infty J(p)\, dp/g. \quad \text{(B8)}$$

The sum of the integrated KE and the Lorentz APE is not exactly conserved and can be produced by two adiabatic nonconservative terms, the volumetric term $J(p)$ related to the nonlinearity of the potential temperature profile and the surface term $S(p)$. The total mass conservation can be written as $\partial_t\langle p_s\rangle = 0$, which implies that $\partial_t\langle\Phi_s p_s\rangle = \partial_t\langle\Phi_s p_s'\rangle$, where $p_s' = p_s - \langle p_s\rangle$. Moreover, since Φ_s does not vary with time, we also have $\partial_t\langle\Phi_s p_s'\rangle = \partial_t\langle\Phi_s(p_s' - \overline{p_s'})\rangle$, where the overbar denotes the temporal

average. We have computed the quantity $\langle \Phi_s(p_s' - \overline{p_s'}) \rangle / g$ and it is very small compared to the horizontally averaged vertically integrated KE and APE. This explains why it is relevant to neglect the topography as done by Lorenz (1955).

REFERENCES

Augier, P., J.-M. Chomaz, and P. Billant, 2012: Spectral analysis of the transition to turbulence from a dipole in stratified fluids. *J. Fluid Mech.,* **713,** 86–108.

Billant, P., and J.-M. Chomaz, 2001: Self-similarity of strongly stratified inviscid flows. *Phys. Fluids,* **13,** 1645–1651.

Boer, G. J., 1982: Diagnostic equations in isobaric coordinates. *Mon. Wea. Rev.,* **110,** 1801–1820.

——, 1983: Homogeneous and isotropic turbulence on the sphere. *J. Atmos. Sci.,* **40,** 154–163.

——, 1989: On exact and approximate energy equations in pressure coordinates. *Tellus,* **41,** 97–108.

——, 1994: Mean and transient spectral energy and enstrophy budgets. *J. Atmos. Sci.,* **51,** 1765–1779.

——, and T. G. Shepherd, 1983: Large-scale two-dimensional turbulence in the atmosphere. *J. Atmos. Sci.,* **40,** 164–184.

——, and S. Lambert, 2008: The energy cycle in atmospheric models. *Climate Dyn.,* **30,** 371–390.

Brune, S., and E. Becker, 2013: Indications of stratified turbulence in a mechanistic GCM. *J. Atmos. Sci.,* **70,** 231–247.

Burgess, B. H., A. R. Erler, and T. G. Shepherd, 2013: The troposphere-to-stratosphere transition in kinetic energy spectra and nonlinear spectral fluxes as seen in ECMWF analyses. *J. Atmos. Sci.,* **70,** 669–687.

Burrows, W., 1976: Diagnostic study of atmospheric spectral kinetic energetics. *J. Atmos. Sci.,* **33,** 2308–2321.

Charney, J. G., 1971: Geostrophic turbulence. *J. Atmos. Sci.,* **28,** 1087–1095.

Cho, J. Y. N., and E. Lindborg, 2001: Horizontal velocity structure functions in the upper troposphere and lower stratosphere: 1. Observations. *J. Geophys. Res.,* **106** (D10), 10 223–10 232.

Deusebio, E., A. Vallgren, and E. Lindborg, 2013: The route to dissipation in strongly stratified and rotating flows. *J. Fluid Mech.,* **720,** 66–103.

Dewan, E. M., 1979: Stratospheric wave spectra resembling turbulence. *Science,* **204,** 832–835.

ECMWF, cited 2010: IFS documentation, version CY36r1. [Available online at http://www.ecmwf.int/research/ifsdocs.]

Fjørtoft, R., 1953: On the changes in the spectral distribution of kinetic energy for two-dimensional, nondivergent flow. *Tellus,* **5,** 225–230.

Frehlich, R., and R. Sharman, 2010: Climatology of velocity and temperature turbulence statistics determined from rawinsonde and ACARS/AMDAR data. *J. Appl. Meteor. Climatol.,* **49,** 1149–1169.

Gage, K. S., 1979: Evidence for a $k^{-5/3}$ law inertial range in mesoscale two-dimensional turbulence. *J. Atmos. Sci.,* **36,** 1950–1954.

Hamilton, K., Y. O. Takahashi, and W. Ohfuchi, 2008: Mesoscale spectrum of atmospheric motions investigated in a very fine resolution global general circulation model. *J. Geophys. Res.,* **113,** D18110, doi:10.1029/2008JD009785.

Kolmogorov, A. N., 1941: The local structure of turbulence in incompressible viscous fluids for very large Reynolds numbers. *C. R. Acad. Sci. (USSR),* **30,** 301–305.

Koshyk, J. N., and K. Hamilton, 2001: The horizontal kinetic energy spectrum and spectral budget simulated by a high-resolution troposphere–stratosphere–mesosphere GCM. *J. Atmos. Sci.,* **58,** 329–348.

Lambert, S., 1984: A global available potential energy-kinetic energy budget in terms of the two-dimensional wavenumber for the FGGE year. *Atmos.–Ocean,* **22,** 265–282.

Lilly, D. K., 1983: Stratified turbulence and the mesoscale variability of the atmosphere. *J. Atmos. Sci.,* **40,** 749–761.

Lindborg, E., 2006: The energy cascade in a strongly stratified fluid. *J. Fluid Mech.,* **550,** 207–242.

——, 2007: Horizontal wavenumber spectra of vertical vorticity and horizontal divergence in the upper troposphere and lower stratosphere. *J. Atmos. Sci.,* **64,** 1017–1025.

——, and G. Brethouwer, 2007: Stratified turbulence forced in rotational and divergent modes. *J. Fluid Mech.,* **586,** 83–108.

Lorenz, E. N., 1955: Available potential energy and the maintenance of the general circulation. *Tellus,* **7,** 157.

Molemaker, M. J., and J. C. McWilliams, 2010: Local balance and cross-scale flux of available potential energy. *J. Fluid Mech.,* **645,** 295–314.

——, ——, and X. Capet, 2010: Balanced and unbalanced routes to dissipation in an equilibrated Eady flow. *J. Fluid Mech.,* **654,** 35–63.

Nastrom, G. D., and K. S. Gage, 1985: A climatology of atmospheric wavenumber spectra of wind and temperature observed by commercial aircraft. *J. Atmos. Sci.,* **42,** 950–960.

Palmer, T., 2001: A nonlinear dynamical perspective on model error: A proposal for non-local stochastic-dynamic parametrization in weather and climate prediction models. *Quart. J. Roy. Meteor. Soc.,* **127,** 279–304.

Schaeffer, N., 2013: Efficient spherical harmonic transforms aimed at pseudo-spectral numerical simulations. *Geochem. Geophys. Geosyst.,* **14,** 751–758.

Shepherd, T. G., 1987: A spectral view of nonlinear fluxes and stationary transient interaction in the atmosphere. *J. Atmos. Sci.,* **44,** 1166–1178.

——, 1993: A unified theory of available potential energy. *Atmos.–Ocean,* **31,** 1–26.

Shutts, G., 2005: A kinetic energy backscatter algorithm for use in ensemble prediction systems. *Quart. J. Roy. Meteor. Soc.,* **131,** 3079–3102.

Siegmund, P., 1994: The generation of available potential energy, according to Lorenz' exact and approximate equations. *Tellus,* **46A,** 566–582.

Skamarock, W. C., 2004: Evaluating mesoscale NWP models using kinetic energy spectra. *Mon. Wea. Rev.,* **132,** 3019–3032.

Smith, S. A., D. C. Fritts, and T. E. Vanzandt, 1987: Evidence for a saturated spectrum of atmospheric gravity waves. *J. Atmos. Sci.,* **44,** 1404–1410.

Steinheimer, M., M. Hantel, and P. Bechtold, 2008: Convection in Lorenz's global energy cycle with the ECMWF model. *Tellus,* **60A,** 1001–1022.

Straus, D., and P. Ditlevsen, 1999: Two-dimensional turbulence properties of the ECMWF reanalyses. *Tellus,* **51A,** 749–772.

Takahashi, Y. O., K. Hamilton, and W. Ohfuchi, 2006: Explicit global simulation of the mesoscale spectrum of atmospheric motions. *Geophys. Res. Lett.,* **33,** L12812, doi:10.1029/2006GL026429.

Tulloch, R., and K. S. Smith, 2009: Quasigeostrophic turbulence with explicit surface dynamics: Application to the atmospheric energy spectrum. *J. Atmos. Sci.,* **66,** 450–467.

Tung, K. K., and W. W. Orlando, 2003: The k^{-3} and $k^{-5/3}$ energy spectrum of atmospheric turbulence: Quasigeostrophic two-level model simulation. *J. Atmos. Sci.,* **60,** 824–835.

Vallgren, A., E. Deusebio, and E. Lindborg, 2011: Possible explanation of the atmospheric kinetic and potential energy spectra. *Phys. Rev. Lett.,* **107,** 268501, 4 pp. [Available online at http://prl.aps.org/abstract/PRL/v107/i26/e268501.]

Vallis, G. K., 2006: *Atmospheric and Oceanic Fluid Dynamics: Fundamentals and Large-Scale Circulation.* Cambridge University Press, 745 pp.

Waite, M. L., 2011: Stratified turbulence at the buoyancy scale. *Phys. Fluids,* **23,** 066602, doi:10.1063/1.3599699.

——, and P. Bartello, 2004: Stratified turbulence dominated by vortical motion. *J. Fluid Mech.,* **517,** 281–308.

——, and C. Snyder, 2009: The mesoscale kinetic energy spectrum of a baroclinic life cycle. *J. Atmos. Sci.,* **66,** 883–901.